Publication V

Ranran Lin, Antti Nestori Laiho, Ari Haavisto, and Antero Arkkio. 2010. End-winding vibrations caused by steady-state magnetic forces in an induction machine. IEEE Transactions on Magnetics, volume 46, number 7, pages 2665-2674.

End-Winding Vibrations Caused by Steady-State Magnetic Forces in an Induction Machine

Ranran Lin[1], Antti Nestori Laiho[2], Ari Haavisto[1], and Antero Arkkio[1]

[1]Department of Electrical Engineering, Faculty of Electronics, Communications and Automation, School of Science and Technology, Aalto University, Espoo, Finland
[2]VTT Technical Research Centre of Finland, Espoo, Finland

We conducted a 3-D electromagnetic analysis coupled with a 3-D mechanical analysis to analyze end-winding vibrations and deformation in an induction machine caused by steady-state magnetic forces on the end winding. Both the analyses were based on the finite-element method. The electromagnetic analysis was used to calculate magnetic forces. During the mechanical analysis, complex support structures in the end region were simplified. We first updated and validated the mechanical model according to a modal model obtained from a modal test, and afterward analyzed deformation, vibrations, and stresses. According to the analysis, the shape of the rotary dynamic deformation of the end winding caused by dynamic forces is similar to the most excitable mode shape though the natural frequency of that mode is much higher than the excitation frequency. The static deformation caused by static forces tends to expand the coil ends outward. Under both types of deformation, the nose portion of the coil ends experiences larger displacement, but von Mises stresses are larger mainly in the knuckle portion.

Index Terms—**End winding, finite-element method, magnetic force, modal testing, vibration.**

I. Introduction

In LARGE radial-flux rotating electric machines, the stator end-winding leakage field can cause time-varying magnetic forces on the end winding [1]–[11], and further, the forces can give rise to forced vibrations [7], [12]–[20]. The stator winding is tightly fixed to the stator core, and therefore the core vibrations may affect the end-winding vibrations [13]. On the other hand, the end-winding vibrations may slightly affect the end-region magnetic field and further the magnetic forces on the end winding. Consequently, the end-region magnetic field and the end-winding vibrations are interactive.

Long-term end-winding vibrations might cause premature winding failure [21], such as the degradation of the insulation integration and the metal fatigue of the materials [15]. In turbogenerators, the three-phase short-circuit current can be 10 times as large as the rated current [16], so relatively large forces may be caused [22], which may aggravate the damage to the end winding. Normally, the end winding is supported so tightly that its vibration level is negligible. However, this may be an expensive solution, and further, the cooling of the end winding may be greatly affected by excessive support structures. Besides, the installation of support structures can change the mechanical structure of the end region, such as natural frequencies and mode shapes. If a certain natural frequency is close to the frequency of the forces and a corresponding mode shape is similar to the spatial distribution of the forces at that frequency, a severe resonance may occur. As a result, it is of importance to model the end-winding vibrations to find optimum support structures.

Manuscript received October 12, 2009; revised December 28, 2009 and February 01, 2010; accepted February 05, 2010. First published March 08, 2010; current version published June 23, 2010. Corresponding author: R. Lin (e-mail: ranran.lin@gmail.com).

Color versions of one or more of the figures in this paper are available online at http://ieeexplore.ieee.org.

Digital Object Identifier 10.1109/TMAG.2010.2044043

Most previous studies are focused on large turbogenerators, possessing similar support structures and coil ends. In [7], natural frequencies of the end winding under different sorts of support structures were analyzed and responses to displacement of the bars were concisely discussed. In [12], strains in the insulation layer of the coil ends were analyzed when the number of spacers between two coil ends was changed and when a fatigue-life test was conducted. Reference [13] revealed that the end-winding vibrations in synchronous generators were stronger under leading power factors than under lagging ones by taking the core vibrations into consideration. In addition, a response model of the end winding was developed in [14] with the use of proportional viscous damping, to identify the most excitable modes and to find effects of the changes and the deterioration of relevant structures. Furthermore, effects of the end-winding vibrations on the insulation and the fatigue of materials used in the coil ends were stated in [15]. In [16], displacement caused by forces on the end winding under short circuit and full load was discussed.

Some studies are concerned with the monitoring of the long-term end-winding vibrations in large turbogenerators [17]–[20]. The state and the condition variables to monitor include voltage, current, vibration signals, etc. Artificial intelligence algorithms, e.g., neural networks, are often employed to analyze those variables. For instance, a feedforward and an auto-associative network were used in [17].

The aforesaid vibrations also exist in large induction motors. Support structures in those motors are normally different from ones in large synchronous generators, since the power of the former is around several MW, whereas the capacity of the latter can reach several hundred MVA. Support structures might be also different among large induction motors made by different manufacturers. However, such a study of the end-winding vibrations in large induction motors the power of which is larger than 1 MW has not been reported yet.

The end-winding vibrations in a 2.24-MW squirrel-cage induction motor were studied. A 3-D electromagnetic and a 3-D mechanical model were built, taking all support structures of

TABLE I
MAIN SPECIFICATIONS OF TEST MACHINE

Parameter	Value
Rated power (MW)	2.24
Full length of stator core (mm)	1000
Outer diameter of stator core (mm)	980
Inner diameter of stator core (mm)	670
Number of pole pairs	2
Number of stator slots	72
Number of turns in series in stator coil	3
Number of parallel branches of stator winding	4
Coil span of stator coil (stator slot pitches)	16

the end winding into account. The two models were coupled in one direction and solved by finite-element method (FEM). Magnetic forces on the end winding obtained from the electromagnetic analysis were used as excitation forces in the mechanical analysis. During the mechanical analysis, the mechanical model was updated according to an experimental modal test. In addition, a procedure for identifying correlated mode pairs (CMPs) of the axisymmetric end winding was proposed and shown to be capable of obtaining accurate values of modal assurance criterion (MAC). In comparison with the previous studies, both static and dynamic deformation as well as stresses caused by a constant and a sinusoidal component of steady-state magnetic forces were studied individually.

II. MODELS AND PROCEDURE FOR ANALYSES

The end region of a three-phase squirrel-cage induction motor equipped with a diamond winding was studied. The diamond winding consisted of form-wound multiturn coils, the detailed description of which can be found in some books and papers, such as [23]–[25]. Inside the stator winding, each coil was made up of three turns in series and each turn consisted of three conductors in parallel. However, in both of the models, the multiturn coils were modeled as single turn coils, and the cross-sectional area of a single turn coil was equal to that of a multiturn coil. Because it was not possible to test the motor under full load in the laboratory, the rotor was removed and only the stator was tested. Table I lists the main parameters of the machine. Fig. 1 shows the electromagnetic model, which incorporated the mechanical model.

A. 3-D Electromagnetic Model

The 3-D electromagnetic model included mainly the end winding and its support structures as well as the air region. Moreover, the core end was included because it could be affected by the stator end-winding leakage [26]. The end shield and the frame were not modeled but they were replaced by standard impedance boundary condition (SIBC) on their inner surface [27], as shown in Fig. 1.

B. 3-D Mechanical Model

The 3-D mechanical model only comprised the end winding and its support structures. The support structures comprised support blocks, strapping tapes, and support rings, as shown in Fig. 4. The support blocks were fixed between two neighboring coil ends to mainly decrease their relative motion in the z- and the φ-direction, where z and φ denote the axial and the circumferential coordinate. The strapping tapes were capable of fastening two neighboring coil ends in the r-direction to mainly decrease their relative motion in the r- and the φ-direction, where r denotes the radial coordinate. The support rings, surrounding all the coil ends, could restrict their motion in the r-direction. The material of the support structures was glass fiber. All the support structures were installed at three different levels in the z-direction, as indicated in Fig. 1. On level 2 are just the support blocks, and on levels 1 and 3 are all the three kinds of support structures.

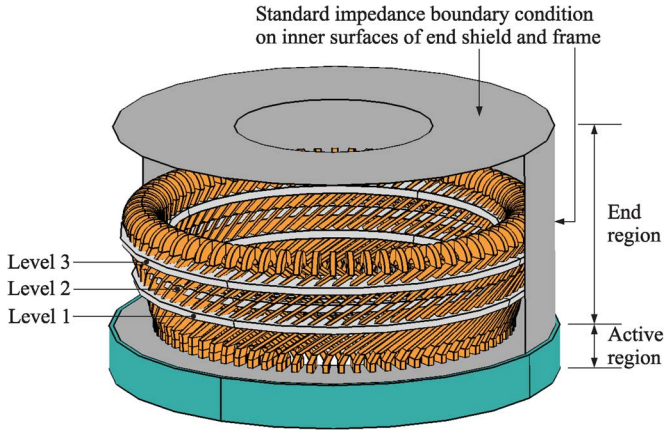

Fig. 1. The 3-D electromagnetic model (with part of the surface of the frame and without the air region) and the 3-D mechanical model incorporated into the electromagnetic model.

It was quite difficult to model the support structures exactly as they were in the machine because of the limited computer resources. In view of their positions, two solid rings were built to model those support structures on levels 1 and 3. The axial length of the ring was equal to that of the support blocks, and the radial length covered both the inner and the outer layer of the winding. Such rings could, to a large extent, possess the same mechanical properties as the support structures in the machine. The support blocks on level 2 were modeled as they were in the machine. Fig. 1 shows clearly the model of those support structures. Besides, the multiturn coils exhibited anisotropic mechanical properties, but the anisotropic properties were supposed to be isotropic in the model because it was difficult to enforce the anisotropic properties in the model.

C. Procedure for Analyses by Finite-Element Method

First, the 3-D electromagnetic model was solved, and the magnetic forces on the end winding were calculated. Next, the calculated forces were used as excitation forces in the 3-D mechanical model, and the end-winding vibrations and the deformation were analyzed.

During the analyses by FEM, effects of the end-winding vibrations and the deformation on the end-region magnetic field were omitted. The magnetomechanical properties of the stator core, e.g., magnetostriction, were not covered. The deformation of the stator teeth was partly caused by the Maxwell forces in

the air gap [28], but it was omitted because the rotor was not included. Hence, the stator core was supposed not to be deformed. In addition, thermal effects causing stresses in the coil ends were not considered.

III. Analyses by Finite-Element Method

A. Analysis of Electromagnetic Model

In the time-harmonic analysis, the stator winding was supplied by a three-phase current source with an rms value $N\tilde{I}_{\rm ph}^{\rm str}/a$, where "$\sim$" over a symbol means the rms value of the field quantity symbolized by the symbol, $I_{\rm ph}^{\rm str}$ denotes stator phase current, N the number of turns in series in the stator coil, and a the number of parallel branches of the stator winding. The governing equation was

$$\nabla \times [\boldsymbol{\nu} \cdot (\nabla \times \underline{\boldsymbol{A}})] + \mathrm{j}\omega\boldsymbol{\sigma} \cdot \underline{\boldsymbol{A}} - \underline{\boldsymbol{J}}_{\rm s} = 0 \tag{1}$$

where "$-$" under a symbol means the complex vector or the phasor of the field quantity symbolized by the symbol, $\boldsymbol{A}$ denotes magnetic vector potential, $\boldsymbol{J}_{\rm s}$ source current density, $\boldsymbol{\nu}$ tensor reluctivity, $\boldsymbol{\sigma}$ tensor conductivity, and ω angular frequency. A linear magnetization curve was adopted in the core. Electric scalar potential ϕ was not solved, because the stator current was known and eddy currents inside the stator coil were omitted owing to the thin conductors there [29]. Besides, the inclusion of ϕ would make the computation problem too large for the computer.

On the inner surface of the frame and the end shield, SIBC also called Leontovich boundary condition given by [30] was enforced

$$\underline{\boldsymbol{E}} - (\boldsymbol{n} \cdot \underline{\boldsymbol{E}})\boldsymbol{n} = Z_{\rm s}\boldsymbol{n} \times \underline{\boldsymbol{H}} \tag{2}$$

where $\boldsymbol{E}$ denotes electric field strength, $\boldsymbol{H}$ magnetic field strength, $\boldsymbol{n}$ a unit normal vector on a boundary, and $Z_{\rm s}$ surface impedance. On the other surfaces, either $\nabla \times \underline{\boldsymbol{A}} \times \boldsymbol{n} = 0$ or $\underline{\boldsymbol{A}} \times \boldsymbol{n} = 0$ was enforced according to the direction of the magnetic induction. A detailed explanation of SIBC can be found in [31].

First-order tetrahedral and prismatic edge elements were employed and the number of degrees of freedom (DOFs) was 973642. The weak formulation of the method of weighted residual (Galerkin's method) was used to construct the system of equations.

B. Analysis of Mechanical Model

The mechanical model was a linear time-invariant (LTI) multi-DOF (MDOF) system. The analysis covered two aspects: free vibration and forced vibration. At first, a free-vibration analysis was conducted to obtain a modal model, and then the modal model was compared with one obtained from a modal test to see whether the calculated modal model ought to be updated or not. The undamped free-vibration analysis was completed according to

$$\boldsymbol{M}\ddot{\boldsymbol{u}} + \boldsymbol{K}\boldsymbol{u} = 0 \tag{3}$$

where $\boldsymbol{M}$ denotes mass matrix, $\boldsymbol{K}$ stiffness matrix, $\boldsymbol{u}$ the column vector of displacement, and "$\ddot{\cdot}$" over a symbol means the second derivative of the field quantity symbolized by the symbol with respect to time.

Next, a forced-vibration analysis was conducted to analyze the static and the dynamic deformation. Because the excitation frequency was much lower than the possible resonant frequency according to the modal test, the damping was omitted. The governing equation was

$$\boldsymbol{M}\ddot{\boldsymbol{u}} + \boldsymbol{K}\boldsymbol{u} = \boldsymbol{f} \tag{4}$$

where $\boldsymbol{f}$ denotes the column vector of force.

In the mechanical model, those surfaces between the coil ends and the coil sides were forced to be stationary, because the modal test revealed that those surfaces were almost fixed. The other surfaces of the model were allowed to move freely.

Second-order tetrahedral nodal elements were employed in both of the analyses, and the number of DOFs was 1 488 882. The way in which the system of equations was constructed was similar to the one mentioned in Section III-A.

IV. Updating and Validation of Models

Validations of the models were completed by measurement, and Fig. 2 shows a diagram of the measurement setup.

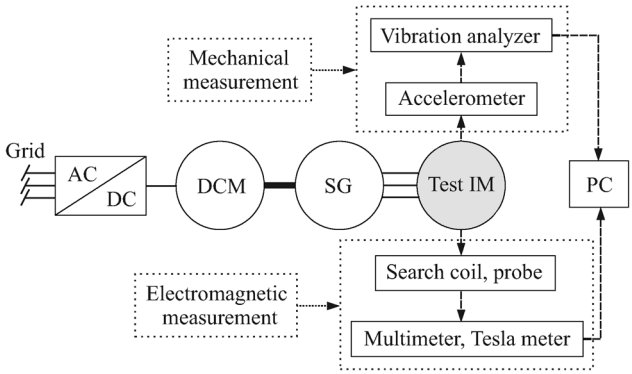

Fig. 2. Diagram of the measurement set-up. DCM: dc motor; SG: synchronous generator; test IM: test induction motor; and PC: personal computer.

A. Validation of Electromagnetic Model

A search coil, made of enameled copper wire, was fixed along a coil end, and its induced electromotive force (EMF) was measured. Magnetic induction was also measured at two points in the end region and in the active region, respectively.

Table II lists calculations and measurements ($\tilde{I}_{\rm ph}^{\rm str} = 1000$ A). In Table II, $\mathcal{E}$ denotes induced EMF, and B_r, B_φ, and B_z the components of magnetic induction. The calculations are

TABLE II
RESULTS OF VALIDATION IN TERMS OF MAGNETIC FIELD

Region	Quantity	Calculation	Measurement
End region	$\tilde{\mathcal{E}}$ (V)	0.71	0.73
	$\tilde{B}_r$ (mT)	28.36	28.3
	$\tilde{B}_\varphi$ (mT)	32.52	33.8
	$\tilde{B}_z$ (mT)	33.73	34.4
Active region	$\tilde{B}_r$ (mT)	59.52	61.4
	$\tilde{B}_\varphi$ (mT)	56.48	54.6
	$\tilde{B}_z$ (mT)	3.92	9.3

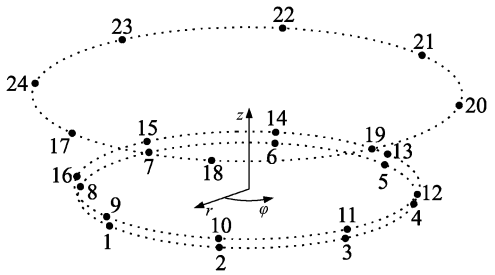

Fig. 3. Measured spots on the coil ends and the stator core end for the impact hammer test.

consistent with the measurements except for B_z at the point in the active region. The reason is that it was difficult to make the probe of the meter exactly perpendicular to the direction of the measured component.

B. Updating and Validation of Mechanical Model

During the validation, an impact hammer test was completed to obtain a modal model. In the 4-pole machine, the wave number of the fundamental of the rotating magnetic field was 2, while that of the fundamental of the steady-state magnetic forces was 4 in the φ-direction. Therefore, at least 8 spots on the end winding evenly distributed in the φ-direction were required for measuring responses to identify the most excitable modes. On account of the 3-D structure, responses were measured on three different axial levels, with eight spots on each level, as indicated in Fig. 3. Spots 1–8 were on the surface of the core end to observe the core vibrations, spots 9–16 were on the surface of the knuckle portion of the coil ends, and spots 17–24 on the surface of the nose portion. Furthermore, a reference spot on the frame was chosen to eliminate effects of the varying operating conditions during the test.

Impact forces with a cut-off frequency 1.2 kHz were exerted on spot 17 from the x-, the y-, and the z-direction. Acceleration at each spot was measured in the corresponding direction by a triaxial piezoelectric accelerometer. A part of the experimental set-up is shown in Fig. 4.

A column of entries in a symmetric frequency response function matrix was obtained during the modal test, which sufficed for obtaining a modal model [32].

After the modal test, experimental mode shapes were compared with nine calculated ones, and values of MAC were computed to identify CMPs. The function of MAC is to provide a

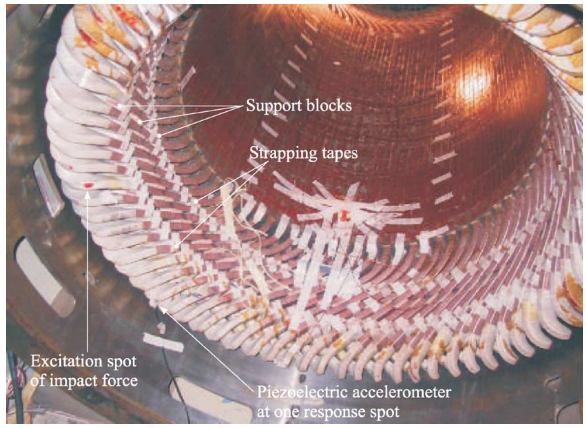

Fig. 4. Part of the experimental set-up for the impact hammer test.

measure of the consistency between estimates of mode shape vectors originating from different sources [33], such as from a numerical computation and from an experimental modal test. MAC is defined as a scalar and is bounded between 0 and 1. A value of 0 means that two compared mode shape vectors are not consistent totally, whereas a value of 1 means that they are exactly consistent. In this paper, values of MAC were computed based on

$$\mathrm{MAC}(\mathrm{calc},\mathrm{exp}) = \frac{\left|\underline{\boldsymbol{\psi}}_{\mathrm{exp}}^{\mathrm{H}}\underline{\boldsymbol{\psi}}_{\mathrm{calc}}\right|^2}{\left(\underline{\boldsymbol{\psi}}_{\mathrm{exp}}^{\mathrm{H}}\underline{\boldsymbol{\psi}}_{\mathrm{exp}}\right)\left(\underline{\boldsymbol{\psi}}_{\mathrm{calc}}^{\mathrm{H}}\underline{\boldsymbol{\psi}}_{\mathrm{calc}}\right)} \tag{5}$$

where $\boldsymbol{\psi}_{\mathrm{exp}}$ and $\boldsymbol{\psi}_{\mathrm{calc}}$ denote experimental and calculated mode shape vector, respectively and "H" near a symbol means the Hermitian transpose of the matrix symbolized by the symbol. $\underline{\boldsymbol{\psi}}_{\mathrm{calc}}$ was computed from (3) relating to the eigenvalues of a matrix. The matrix of eigenvalues, $\boldsymbol{\Lambda}$, and that of corresponding eigenvectors, i.e., mode shape vectors, $\boldsymbol{\Psi}$, were written as $\boldsymbol{\Lambda} = \mathrm{diag}(\omega_{1,\mathrm{calc}}^2,\cdots,\omega_{9,\mathrm{calc}}^2)$ and $\boldsymbol{\Psi} = (\boldsymbol{\psi}_{1,\mathrm{calc}},\cdots,\boldsymbol{\psi}_{9,\mathrm{calc}})$, respectively, where $\omega_{i,\mathrm{calc}}^2$ and $\boldsymbol{\psi}_{i,\mathrm{calc}}$ denote the eigenvalue and the corresponding eigenvector of mode i, $i = 1,\cdots,9$.

The end winding was almost axisymmetric, so calculated mode shapes were not fixed and they could be shifted in the φ-direction. However, experimental mode shapes were fixed on account of the fixed measured spots. Therefore, at first, those points lying at the position of the measured spots in Fig. 3 were chosen in the model. Mode shape vectors were calculated based on those positions, and then values of MAC were computed. Next, those points for calculating mode shapes were shifted by a stator slot pitch, i.e., 5°, in the φ-direction. Mode shape vectors were calculated again based on the updated positions, and values of MAC were computed again. The shift in calculated positions was not halted until 72 slot pitches were shifted, and values of MAC were computed under each shift. During those shifts, experimental mode shape vectors were kept constant.

Usually mode shapes of the end winding are viewed from the z-direction, for variations in the r- and the φ-direction are more interesting. Because the end winding was a cylindrical structure to some extent, it would be convenient to describe its

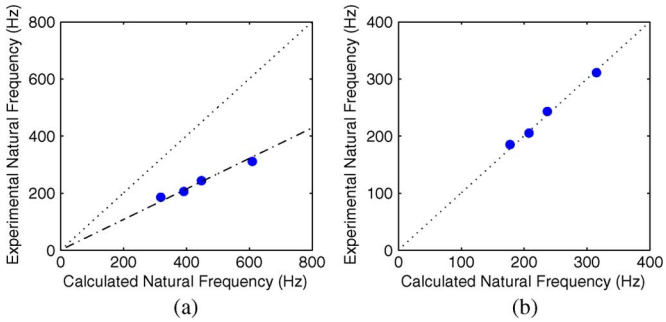

Fig. 5. Comparisons of CMPs before and after the model updating. (a) Before the model updating. (b) After the model updating.

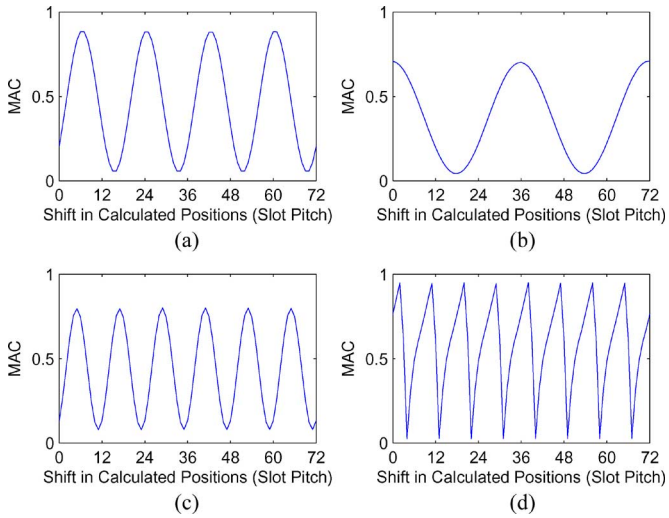

Fig. 6. Values of MAC as a function of circumferential shift in the calculated positions. (a) CMP 1. (b) CMP 2. (c) CMP 3. (d) CMP 4.

mode shapes by the wave number k of ring modes of a cylindrical structure in the φ-direction [34]. Among the above calculated modes, there existed double modes which had equal natural frequencies due to repeated roots of the characteristic equation [35], and one mode shape the wave number of which was k could be obtained by rotating the other one by $90^\circ/k$ in the φ-direction. The existence of double modes is commonplace in many structures [35].

A comparison is plotted in Fig. 5(a). It is evident that the points lie on the dash-dotted line, the slope of which is not 1. The most possible reason was erroneous material properties according to [35]. The calculated natural frequencies are systematically almost twice as high as the corresponding experimental ones, which indicates that the mechanical model required being updated to make the points in Fig. 5(a) concentrated on a line the slope of which is 1 and to make values of MAC for all CMPs as close to 1 as possible.

In fact, natural frequencies of a mechanical structure are related mainly to its geometric shape, mass, stiffness, and boundary conditions. Moreover, numerical computations of natural frequencies may be affected by the set-up of numerical models, such as the order of elements and the structure of a mesh. However, the set-up of that mechanical model was considered fixed during the model updating. According to [32], the geometric shape of the mechanical model proved reasonable, for the points in Fig. 5(a) are concentrated on a line instead of being scattered irregularly around a line. The mass and the boundary conditions of the model were set up according to the real end winding and the real physical situation. Therefore, the stiffness was the parameter to revise.

As discussed in Section II, because of the limitations of the modeling conditions, the multiturn stator coils were simplified as homogeneous single turn coils, and a combination of different support structures made of glass fiber was also simplified as two solid rings. Therefore, the whole mechanical model was, to some extent, different from the real structure and exhibited stronger stiffness than the real structure. The above calculated natural frequencies were inaccurate when original mechanical properties of the materials were still used.

In general, the modal stiffness of a solid body is determined by its material properties such as the Young's modulus and the Poisson's ratio, its geometric structure, and its boundary conditions. As a matter of fact, the geometric structure and the boundary conditions of the mechanical model have been discussed above, so the main parameters to revise should be the mechanical properties. To find sensitivity of the natural frequencies to the material properties, a series of simulations were completed, in which the Young's moduli and the Poisson's ratios were changed respectively. By comparison, it was found that Young's modulus played a much more important role in dominating the natural frequencies than Poisson's ratio, so Young's modulus was the main parameter to revise. Therefore, the Young's modulus of copper was decreased from 128 GPa to 33 GPa, and that of glass fiber was from 80 GPa to 20 GPa. To make values of MAC as high as possible, the Poisson's ratios were also revised slightly.

After the model updating, a calculated modal model was compared with the experimental one again. Values of MAC as a function of circumferential shift in calculated positions were shown in Fig. 6. All the values of MAC fluctuate periodically according to circumferential shift, and the fluctuation periods are dependent upon the aforementioned wave number k. In Fig. 6, only the maximum values of MAC have practical meaning for the CMPs, and the maxima for CMPs 1–4 are 0.88, 0.72, 0.80, and 0.95, respectively. Though they are not equal to 1, those values still indicate that the calculated mode shapes were, to a large extent, consistent with the experimental ones, since it was difficult to make all the aforesaid values of MAC equal to 1 for this complex structure. Actually, the aforementioned CMPs 1–4 were determined according to Fig. 7, which shows values of MAC for different combinations. Those combinations whose values of MAC are close to 1 were regarded as CMPs, so there were eight combinations in total, as shown by the eight tall blocks in Fig. 7. However, because calculated modes 1–2, 3–4, 5–6, and 8–9 were double modes, only one of them was included. Hence, there were eventually four CMPs, as mentioned above. What needs to be mentioned is that calculated mode 7 was not found clearly in the modal test, and the reason might be its high modal damping. Furthermore, Fig. 5(b) plots a comparison after the updating, and the points lie mainly on the dotted line, the slope of which is 1.

TABLE III
COMPARISON OF TWO MODAL MODELS

Calculated modal model		Experimental modal model		
Mode number	Natural frequency (Hz)	Mode number	Natural frequency (Hz)	Modal damping
1, 2	178.5	1	184.7	0.78%
3, 4	208.3	2	205.2	0.88%
5, 6	238.9	3	243.2	1.11%
7	263.3	—	—	—
8, 9	315.6	4	311.1	1.62%

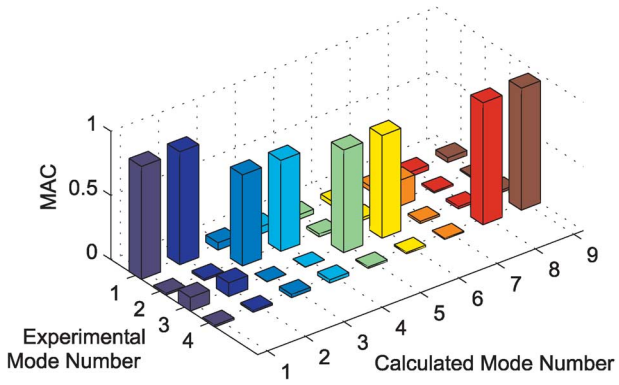

Fig. 7. Values of MAC for different combinations of the experimental modes and the calculated modes.

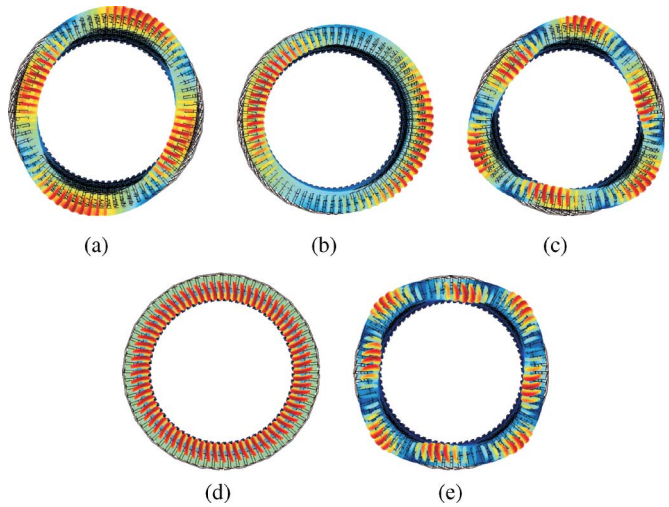

Fig. 8. Views of the calculated mode shapes correlating with lower natural frequencies from the z-direction. Warm colors: large relative amplitude; cool colors: small relative amplitude. (a) Mode 1 ($k = 2$). (b) Mode 3 ($k = 1$). (c) Mode 5 ($k = 3$). (d) Mode 7 ($k = 0$). (e) Mode 8 ($k = 4$).

V. RESULTS AND ANALYSIS

A. Calculated and Experimental Modal Model

The undamped mode shapes correlating with lower natural frequencies are shown in Fig. 8. With respect to those double modes, only one of them was shown. The mode shape of mode 8 ($k = 4$) in Fig. 8(e) corresponds to the steady-state magnetic forces in the 4-pole machine.

The calculated modal model was compared with the experimental one, as shown in Table III. In the experimental modal model, modal damping was supposed and no point damping was considered. As a matter of fact, it was difficult to find certain modes with high modal damping during the modal test. The natural frequency of mode 8 or mode 9 ($k = 4$), which corresponds to the magnetic forces, is 315.6 Hz, which is much higher than the excitation frequency, 100 Hz, so the damping does not have an important effect on the forced vibrations.

B. Magnetic Forces and Deformation

Magnetic forces on the stator end winding were classified as Lorentz force [22], and the force density $\boldsymbol{f}$ was defined by $\boldsymbol{f} = \boldsymbol{J} \times \boldsymbol{B}$, where $\boldsymbol{J}$ and $\boldsymbol{B}$ denote current density and magnetic induction, respectively. Under the time-harmonic analysis, the magnetic force density in the coil ends was

$$\begin{cases} f_r = f_{r,-} + f_{r,\sim} = f_{r,-} + \hat{f}_{r,\sim}\cos(2\omega_s t + \vartheta_{r0}) \\ f_\varphi = f_{\varphi,-} + f_{\varphi,\sim} = f_{\varphi,-} + \hat{f}_{\varphi,\sim}\cos(2\omega_s t + \vartheta_{\varphi 0}) \\ f_z = f_{z,-} + f_{z,\sim} = f_{z,-} + \hat{f}_{z,\sim}\cos(2\omega_s t + \vartheta_{z0}) \end{cases} \quad (6)$$

where "$\wedge$" over a symbol means the amplitude of the field quantity symbolized by the symbol, f_r, f_φ, and f_z denote the force components, $f_{r,-}$, $f_{\varphi,-}$, and $f_{z,-}$ the constant components, $f_{r,\sim}$, $f_{\varphi,\sim}$, and $f_{z,\sim}$ the sinusoidal components, ϑ_{r0}, $\vartheta_{\varphi 0}$, and ϑ_{z0} the phase angles, ω_s the angular frequency of the stator field, and t time. Obviously, each force density component consisted of a constant component and a double-frequency sinusoidal component, so the force also comprised a static and a dynamic component. Because of the LTI characteristic, the above two components were tackled individually.

The static components, $f_{r,-}$, $f_{\varphi,-}$, and $f_{z,-}$, would not lead to vibrations but static deformation. The magnitude of the static force density $|\boldsymbol{f}_-|$ was calculated by

$$|\boldsymbol{f}_-| = \sqrt{f_{r,-}^2 + f_{\varphi,-}^2 + f_{z,-}^2}. \quad (7)$$

Fig. 9 shows the distribution of $|\boldsymbol{f}_-|$. In Fig. 9, every phase belt comprising six stator coils experiences the same static forces. In the coil ends except the portion close to the core, relatively large force density in each phase belt appears in the involute portion of the first coil end along the direction of the rotating magnetic field, and the force density gets smaller in the rest of the coil ends. The force density in the involute and the knuckle portion

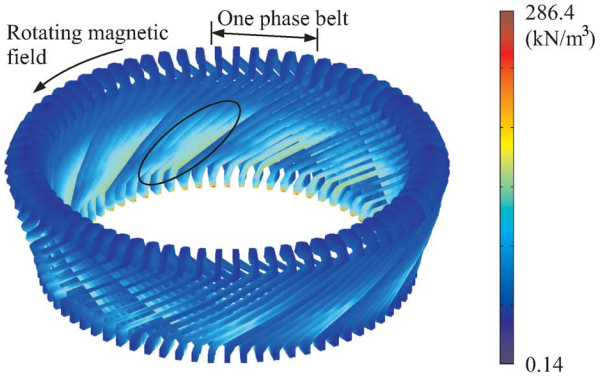

Fig. 9. Distribution of $|\boldsymbol{f}_{-}|$ in the stator end winding.

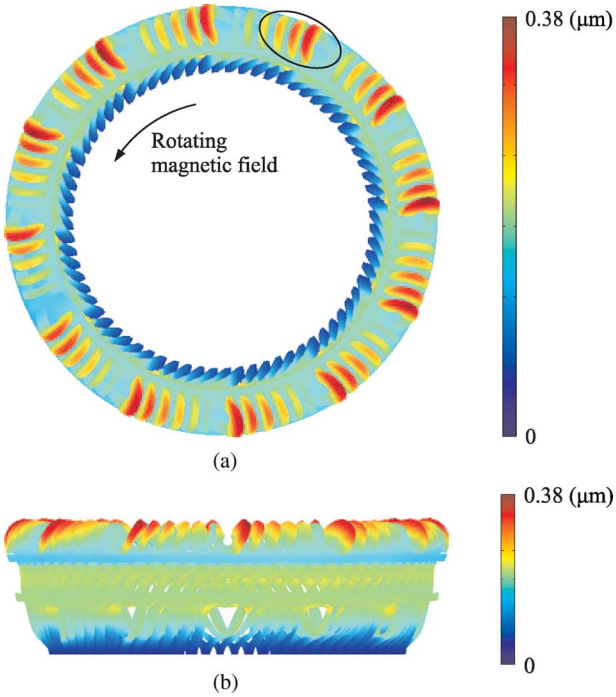

Fig. 10. Static deformation caused by $f_{r,-}$, $f_{\varphi,-}$, and $f_{z,-}$. (a) View from the z-direction. (b) View from the r-direction.

of the coil ends, marked by the ellipse, is much larger than the one in the nose portion.

The deformation was dependent on displacement at each of the nodal points. Fig. 10 shows the static deformation caused by $f_{r,-}$, $f_{\varphi,-}$, and $f_{z,-}$. It is visible that the end winding is expanded outward due to the static forces. The deformation of the nose portion of the first coil end is stronger than that of the nose portion of the other coil ends in a phase belt, and the maximum displacement is 3.8×10^{-7} m. Although the involute and the knuckle portion experience larger static forces, strong static deformation appears at the nose portion, as marked by the ellipse in Fig. 10(a).

The dynamic components, $f_{r,\sim}$, $f_{\varphi,\sim}$, and $f_{z,\sim}$, would lead to forced vibrations, which might cause a resonance. The magnitude of the dynamic force density $|\boldsymbol{f}_{\sim}|$ at a certain instant was calculated by

$$|\boldsymbol{f}_{\sim}| = \sqrt{f_{r,\sim}^2 + f_{\varphi,\sim}^2 + f_{z,\sim}^2}. \tag{8}$$

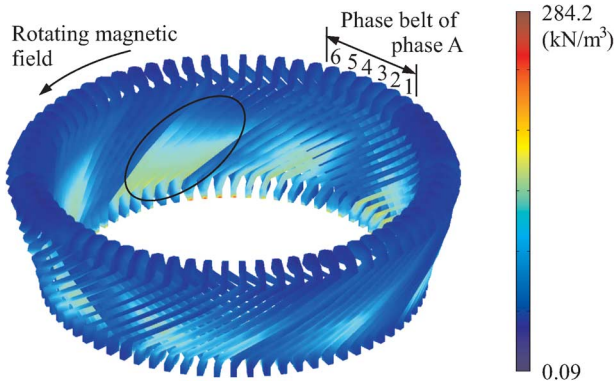

Fig. 11. Distribution of $|\boldsymbol{f}_{\sim}|$ in the stator end winding.

Fig. 11 shows the distribution of $|\boldsymbol{f}_{\sim}|$ at the instant when the current of phase A reaches the maximum. The distribution of $|\boldsymbol{f}_{\sim}|$ rotates in the same direction as the magnetic field. Though the current of phase A reaches the maximum in Fig. 11, relatively large dynamic force density does not appear in the phase belt of phase A. Like the static forces, in the coil ends except the portion close to the core, the involute and the knuckle portion experience larger dynamic forces than the nose portion, as marked by the ellipse.

The corresponding deformation based on the computation of operating deflection shapes is illustrated in Fig. 12. Though $|\boldsymbol{f}_{\sim}|$ is larger in the involute and the knuckle portion, stronger deformation appears at the nose portion, as marked in Fig. 12(a) by the ellipse with a solid line. The maximum displacement in the forced vibrations is 5.1×10^{-7} m. In addition, the deformation of the nose portion of the coil ends in two successive phase belts is in the opposite direction at a certain instant, as shown by the ellipse with a dash line. In a phase belt, e.g., the one indicated in Fig. 11, the dynamic deformation at the nose portion of coil ends 1–6 is also different. Fig. 13 shows the magnitude of displacement of each coil end as a function of solution angle, and it can be seen that the nose portion of the outermost coil ends 1 and 6 experiences larger displacement than that of the other four coil ends. Due to the rotary distribution of $|\boldsymbol{f}_{\sim}|$, the deformation also rotates in the same φ-direction. Another important phenomenon is that the dynamic deformation correlates with the mode shape of mode 8 or mode 9 $(k = 4)$, though the excitation frequency, 100 Hz, is much lower than the natural frequency of mode 8 or 9, 315.6 Hz.

C. Real-Time Measurement of Forced Vibrations

During the measurement of forced vibrations, the supply voltage varied at a frequency of 50 Hz, and real-time acceleration at spots 17–24 marked in Fig. 3 was measured by eight triaxial piezoelectric accelerometers.

Acceleration at spots 1–16 was not measured since vibration levels at those spots were small by comparison with those at spots 17–24. By integrating the acceleration twice, corresponding displacement was obtained. Only under the dynamic forces did the acceleration exist, so the displacement obtained correlated with the dynamic forces. The components of the displacement at spot 20, and the discrete Fourier transform (DFT) of those components based on an algorithm of fast Fourier transform, are shown in Fig. 14. In fact, measurements of the displacement based on 100-Hz components were around

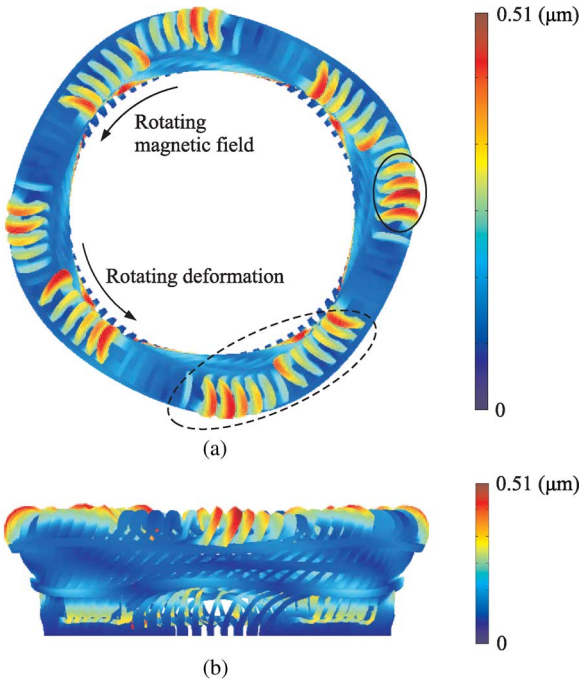

Fig. 12. Dynamic deformation caused by $f_{r,\sim}$, $f_{\varphi,\sim}$, and $f_{z,\sim}$. (a) View from the z-direction. (b) View from the r-direction.

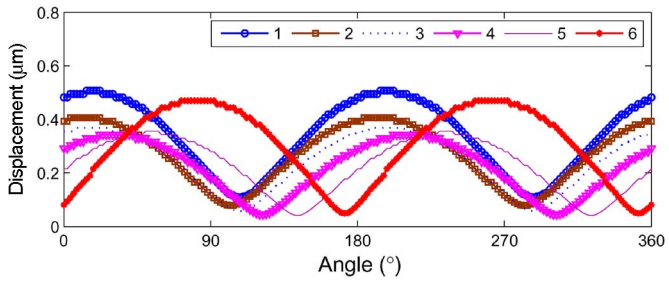

Fig. 13. Calculated magnitude of displacement at the nose portion of each coil end in a phase belt as a function of solution angle.

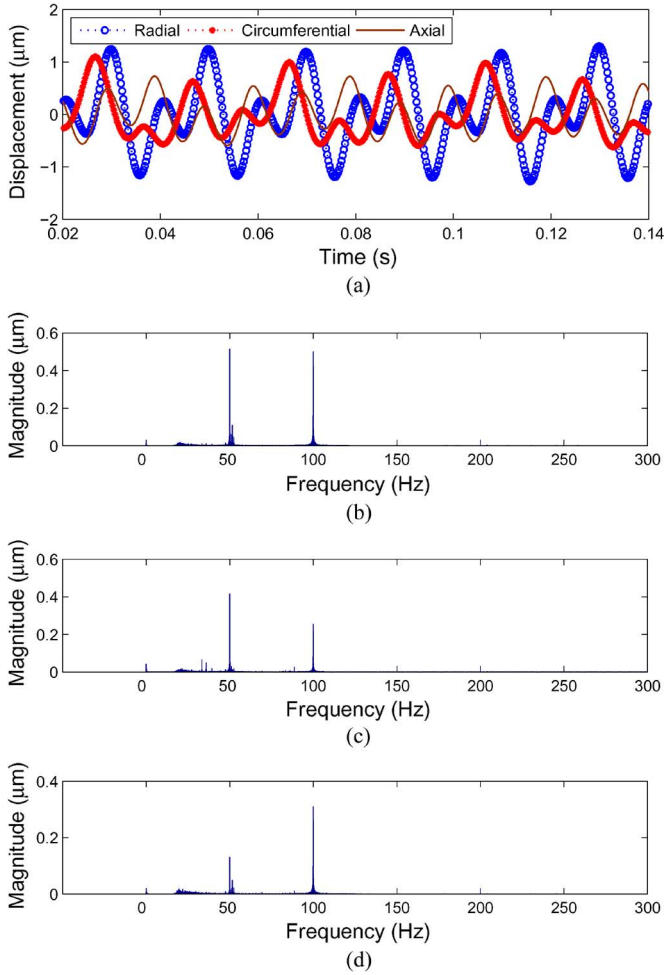

Fig. 14. Time-domain and frequency-domain analysis of the displacement. (a) The components of the displacement at spot 20 in the time domain. (b) The DFT of the radial displacement. (c) The DFT of the circumferential displacement. (d) The DFT of the axial displacement.

10%–30% larger than calculations at all the spots, which might result from the following two aspects. One is that the end-region magnetic field and the end-winding vibrations were interactive but the interaction was not covered in the calculation by FEM, and the other is that the structure of the end winding was not exactly axisymmetric due to manufacture but the calculation used an exactly axisymmetric model. In addition to the expected 100-Hz components, in Fig. 14, notable 50-Hz components are found. Actually, 50-Hz components were detected in all the measured spots, and they had a considerable effect on the time-domain waveforms.

To find the reason for the 50-Hz components, similar measurement was completed, in which the supply voltage varied at a frequency of 25 Hz. Under the circumstances, the sinusoidal components of the forces should vary at a frequency of 50 Hz. After checking the DFT of the components of displacement, notable 25-Hz components were found in the frequency domain. Therefore, the presence of the 25-Hz and the aforementioned 50-Hz components resulted from the measurement. The electromagnetic sensitivity of the accelerometers was 1.4 g/T, where g denotes the acceleration of gravity. And the electromagnetic sensitivity was regarded as the main reason. In addition, there was a 4.7-mA dc current inside the connection wire, and that it interacted with the time-varying magnetic field caused forces on the wire, which also affected the measurements.

D. Stresses

The von Mises criterion is one of the yield criteria for ductile materials [36]. Corresponding von Mises stresses τ_{v}, i.e., equivalent scalar stresses expressed by principal stresses, were calculated in the mechanical model by

$$\tau_{\mathrm{v}} = \sqrt{\frac{(\tau_1-\tau_2)^2+(\tau_2-\tau_3)^2+(\tau_3-\tau_1)^2}{2}} \tag{9}$$

where τ_1, τ_2, and τ_3 denote principal stresses. Under the static deformation, the maximum τ_{v} was 0.096 MPa, and under the dynamic deformation, the maximum τ_{v} was 0.111 MPa. In both the cases, the maxima appeared in the knuckle portion of the coil ends. Compared with the yield strength of copper, 69 MPa, the maxima were small.

Metal fatigue, on account of repeated stresses in copper conductors of the end winding, was also evaluated. Because the magnetic forces on the end winding were like fluctuating loads, corresponding stresses could be divided into mean stress and

alternating stress. Goodman relationship, accounting for effects of mean stress on the fatigue life of a material [37], was used according to [38] by

$$\hat{\tau} = \tau_{\mathrm{fs}} \left(1 - \frac{\overline{\tau}}{\tau_{\mathrm{ts}}} \right) \tag{10}$$

where "−" over a symbol means the mean of the field quantity symbolized by the symbol, τ denotes stress, τ_{fs} the desired fatigue strength for zero mean stress, and τ_{ts} the tensile stress of a material. In most of the literature, copper was regarded as a metal without an obvious endurance limit [38]. Moreover, different types of copper have different S-N curves also called Wöhler curves, such as annealed copper and stretched copper [39], and their fatigue strength can also be affected by temperature and pressure [40]. In this paper, mechanical properties of annealed copper were used. τ_{fs} and τ_{ts} were 75 MPa and 220 MPa, respectively. Inside the copper conductors, the maximum level of calculated mean and alternating stress was in a magnitude of 0.01 MPa, which was much smaller than τ_{fs} and τ_{ts}. Therefore, when the mean and the alternating stresses were taken into (10), their points in the $\overline{\tau} - \hat{\tau}$ plane of a Goodman diagram were definitely below the Goodman line.

VI. Conclusions and Discussions

This paper gives a deeper understanding of end-winding vibrations in a large induction motor. End-winding vibrations caused by the steady-state magnetic forces and corresponding deformation are analyzed based on a 3-D electromagnetic analysis coupled with a 3-D mechanical analysis. The analyses are carried out by FEM and both are validated.

The spatial distribution of the static deformation, due to the static magnetic forces, is the same in every phase belt, but in a phase belt, different coil ends have different degrees of deformation. There is strong static deformation at the nose portion of the coil ends, but von Mises stresses in the knuckle portion are larger. On the other hand, the dynamic magnetic forces cause forced vibrations and further dynamic deformation. The deformation is rotary in the circumferential direction. And its spatial distribution, to some extent, correlates with the mode shape the wave number of which is equal to that of the forces, although the excitation frequency is much lower than the natural frequency of that mode. Like the static deformation, the nose portion of the coil ends experiences stronger deformation, but relatively large von Mises stresses are found in the knuckle portion. The maximum von Mises stresses are absolutely small in comparison with the yield strength of copper, and the points of the mean and the alternating stresses are far below the Goodman line in a Goodman diagram. As a result, the metal fatigue of the copper conductors is not important.

The mode shapes of the end winding of the induction motor correlating with lower natural frequencies are similar to those of large turbogenerators. However, the overall levels of the end-winding steady-state vibrations are small, by comparison with those in large turbogenerators reported in such as [13], [16]. Furthermore, effects of the core vibrations on the end-winding vibrations can be omitted in the induction motor, but those effects need to be considered in some large turbogenerators as reported in [13].

In fact, the end region is the most complex structure in large induction machines, and it has to be analyzed in 3-D space. To study the end-region magnetic field and the end-winding vibrations, 3-D analyses based on FEM, currently, are the most appropriate means. However, even if modern computers are powerful, such 3-D analyses are still challenging, and some assumptions and simplifications are still required. For instance, in the models, the nonlinear magnetization characteristic of the core and the nonlinear mechanical properties are not covered; the complex support structures of the end winding are simplified, etc. Therefore, validations, as well as further model updating, are necessary for both the electromagnetic and the mechanical model. It is well known that time-dependent analyses by FEM can give more accurate results for nonlinear models, but, for models of the end region, they are extremely time-consuming and require plenty of computer resources. Hence, when nonlinearity in the end region is not strong, time-harmonic analyses based on FEM are a relatively fast and accurate method for electromagnetic and mechanical analysis of the end region.

Acknowledgment

This work was supported by Finnish Foundation for Technology Promotion and by Aalto University, Finland. The authors thank J. Roivainen, T. Holopainen, and J. Järvinen from ABB Corporation in Helsinki, Finland for making some comments on this paper. The authors also thank ABB Corporation in Finland for providing the test electric machine, and VTT Technical Research Centre of Finland for providing devices for the vibration measurement.

References

[1] J. F. Calvert, "Forces in turbine generator stator windings," *Trans. AIEE*, vol. 50, no. 1, pp. 178–194, Mar. 1931.

[2] J. A. Tegopoulos, "Forces on the end winding turbine-generators II—Determination of forces," *IEEE Trans. Power App. Syst.*, vol. PAS-85, no. 2, pp. 114–122, Feb. 1966.

[3] D. J. Scott, S. J. Salon, and G. L. Kusik, "Electromagnetic forces on the armature end windings of large turbine generators I—Steady state conditions," *IEEE Trans. Power App. Syst.*, vol. PAS-100, no. 11, pp. 4597–4603, Nov. 1981.

[4] S. J. Salon, D. J. Scott, and G. L. Kusic, "Electromagnetic forces on the end windings of large turbine generators. II. Transient conditions," *IEEE Trans. Power App. Syst.*, vol. PAS-102, no. 1, pp. 14–19, Jan. 1983.

[5] G. K. M. Khan, G. W. Buckley, and N. Brooks, "Calculation of forces and stresses on generator end-windings—Part I: Forces," *IEEE Trans. Energy Convers.*, vol. 4, no. 4, pp. 661–670, Dec. 1989.

[6] X. Wen, R. Yao, and J. A. Tegopoulos, "Calculation of forces on the stator end windings of turbogenerator by the transient quasi-3D method," *IEEE Trans. Magn.*, vol. 32, no. 3, pp. 1669–1672, May 1996.

[7] A. Merkhouf, B. F. Boueri, and H. Karmaker, "Generator end windings forces and natural frequency analysis," in *Proc. IEEE Int. Electric Machines and Drives Conf.*, Jun. 2003, vol. 1, pp. 111–114.

[8] K.-C. Kim, H.-W. Lee, Y.-D. Chun, and J. Lee, "Analysis of electromagnetic force distribution on end winding for motor reliance," *IEEE Trans. Magn.*, vol. 41, no. 10, pp. 4072–4074, Oct. 2005.

[9] Y. Liu and S. Hjärne, "Analysis of forces on coil ends of formed stator windings," in *Proc. Int. Conf. Electrical Machines and Systems*, Seoul, Korea, Oct. 2007, pp. 1019–1024.

[10] R. Lin and A. Arkkio, "3-D finite element analysis of magnetic forces on stator end-windings of an induction machine," *IEEE Trans. Magn.*, vol. 44, no. 11, pp. 4045–4048, Nov. 2008.

[11] R. D. Stancheva and I. I. Iatcheva, "3-D electromagnetic force distribution in the end region of turbogenerator," *IEEE Trans. Magn.*, vol. 45, no. 3, pp. 1000–1003, Mar. 2009.

[12] M. Ohtaguro, K. Yagiuchi, and H. Yamaguchi, "Mechanical behavior of stator endwindings," *IEEE Trans. Power App. Syst.*, vol. PAS-99, no. 3, pp. 1181–1185, May/Jun. 1980.
[13] M. R. Patel and J. M. Butler, "End-winding vibrations in large synchronous generators," *IEEE Trans. Power App. Syst.*, vol. PAS-102, no. 5, pp. 1371–1377, May 1983.
[14] A. C. Léger and N. Szylowicz, "Modelling the vibration behaviour of stator end windings," in *Proc. 8th Int. Conf. Electrical Machines and Drives*, Cambridge, U.K., Sep. 1997, pp. 160–164.
[15] J. Zhang, X. Jiang, and Z. You, "Vibration measurement of the generator stator end windings and precautions against insulation wearing," in *Proc. Int. Conf. Power System Technology*, Beijing, China, Aug. 1998, vol. 2, pp. 1021–1024.
[16] O. Drubel, S. Kulig, and K. Senske, "End winding deformations in different turbo generators during 3-phase short circuit and full load operation," *Electr. Eng.*, vol. 82, no. 3–4, pp. 145–152, Mar. 2000.
[17] E. M. P. van Wyk and A. J. Hoffman, "Detecting long-term trends in turbo-generator stator end-winding vibrations through neural network modelling," *J. Sound Vibr.*, vol. 253, no. 3, pp. 529–544, Jun. 2002.
[18] J. Demcko, J. Velotta, and A. Tesla, "New tools to monitor critical vibration of end-windings in turbo-generators," in *Proc. IEEE Int. Electric Machines and Drives Conf.*, Antalya, Turkey, May 2007, pp. 1020–1024.
[19] R. Sewak, R. Ranjan, and A. K. L. Rao, "Intricate aspects of turbogenerator endwinding vibration monitoring based on data analysis," in *Proc. Int. Conf. Condition Monitoring and Diagnosis*, Beijing, China, Apr. 2008, pp. 130–135.
[20] D. Shally, M. Farrell, and K. Sullivan, "Generator end winding vibration monitoring," in *Proc. 43rd Int. Univ. Power Engineering Conf.*, Padova, Italy, Sep. 2008, pp. 1–5.
[21] G. Klempner and I. Kerszenbaum, *Operation and Maintenance of Large Turbo-Generators*. Hoboken, NJ: Wiley, 2004.
[22] S. J. Salon, "Finite element analysis of electric machinery," *IEEE Comput. Appl. Power*, vol. 3, no. 2, pp. 29–32, Apr. 1990.
[23] M. T. Holmberg, "Three-Dimensional Finite Element Computation of Eddy Currents in Synchronous Machines," Ph.D. dissertation, Chalmers Univ. Technol., Gothenberg, Sweden, Dec. 1998.
[24] W. Tong, "Numerical analysis of flow field in generator end-winding region," *Int. J. Rotat. Mach.*, vol. 2008, pp. 1–10, 2008.
[25] D. Ban, D. Žarko, and I. Mandić, "Turbogenerator end-winding leakage inductance calculation using a 3-D analytical approach based on the solution of Neumann integrals," *IEEE Trans. Energy Convers.*, vol. 20, no. 1, pp. 98–105, Mar. 2005.
[26] R. Lin and A. Arkkio, "Calculation and analysis of stator end-winding leakage inductance of an induction machine," *IEEE Trans. Magn.*, vol. 45, no. 4, pp. 2009–2014, Apr. 2009.
[27] R. Lin, A. Haavisto, and A. Arkkio, "Validation of a time-harmonic numerical model for solving magnetic field in end region of a radial-flux machine," *IEEE Trans. Magn.*, vol. 45, no. 12, pp. 5360–5367, Dec. 2009.
[28] S. Somkun, A. J. Moses, and P. I. Anderson, "Effect of magnetostriction anisotropy in nonoriented electrical steels on deformation of induction motor stator cores," *IEEE Trans. Magn.*, vol. 45, no. 10, pp. 4744–4747, Oct. 2009.
[29] A. Arkkio, "Analysis of Induction Motors Based on the Numerical Solution of the Magnetic Field and Circuit equations," Ph.D. dissertation, Helsinki Univ. Technol., Espoo, Finland, Dec. 1987.
[30] P. Alotto, A. De Cian, G. Molinari, and M. Rossi, "Implementation of surface impedance boundary conditions in the cell method via the vector fitting technique," *COMPEL: Int. J. Comput. Math. Elect. Electron. Eng.*, vol. 26, no. 3, pp. 859–872, 2007.
[31] D. J. Hoppe and Y. Rahmat-Samii, *Impedance Boundary Conditions in Electromagnetics*. Washington, DC: Taylor & Francis, 1995.
[32] J. He and Z. Fu, *Modal Analysis*. Oxford, U.K.: Butterworth-Heinemann, 2001.
[33] R. J. Allemang, "The modal assurance criterion—Twenty years of use and abuse," *Sound Vibr.*, vol. 37, no. 8, pp. 14–21, Aug. 2003.
[34] C. K. Mechefske and F. Wang, "Theoretical, numerical, and experimental modal analysis of a single-winding gradient coil insert cylinder," *Magn. Reson. Mater. Phy.*, vol. 19, no. 3, pp. 152–166, Aug. 2006.
[35] D. J. Ewins, *Modal Testing: Theory, Practice and Application*, 2nd ed. Hertfordshire, U.K.: Research Studies, 2000.
[36] F. P. Beer, E. R. Johnston, Jr., J. T. DeWolf, and D. F. Mazurek, *Mechanics of Materials*, 5th ed. New York: McGraw-Hill, 2009.
[37] R. W. Hertzberg, *Deformation and Fracture Mechanics of Engineering Materials*, 3rd ed. New York: Wiley, 1989.
[38] D. R. Askeland and P. P. Phulé, *The Science and Engineering of Materials*, 4th ed. Pacific Grove, CA: Brooks/Cole, 2003.
[39] J. Awatani, K. Katagiri, A. Omura, and T. Shiraishi, "A study of the fatigue limit of copper," *Metallurgical Trans. A*, vol. 6A, no. 5, pp. 1029–1034, May 1975.
[40] V. F. Udovenko, A. I. Alekseev, L. F. Yakovenko, and I. M. Lyubarskii, "Fatigue strength of copper under cyclic loading conditions at low temperature and in vacuum," *Metal Sci. Heat Treat.*, vol. 9, no. 9, pp. 697–699, Sep. 1967.

Ranran Lin (S'09) was born in Beijing, China, in 1980. He received the B.Sc. degree in engineering from Shanghai Jiao Tong University, Shanghai, China, in 2002, and the M.Sc. degree in technology from Helsinki University of Technology, Espoo, Finland, in 2004.

He is a Research Scientist with the Department of Electrical Engineering, Faculty of Electronics, Communications, and Automation, School of Science and Technology, Aalto University, Espoo. His current research interests include 3-D numerical analysis of the electromagnetic field and mechanical vibration in the end region of large rotating electric machines.

Mr. Lin served as Session Chair of 2008 IEEE International Magnetics Conference held in Madrid, Spain. He is a Member of International Compumag Society (ICS). He won the 2009 Chinese Government Award for Outstanding Self-Financed Students Abroad.

Antti Nestori Laiho was born in Helsinki, Finland, in 1977. He received the M.Sc. (Tech.) degree and the D.Sc. (Tech.) degree from Helsinki University of Technology, Espoo, Finland, in 2003 and 2009, respectively.

He is a Research Scientist with VTT Technical Research Centre of Finland, Espoo. His research interests involve electromechanical interactions, structural analysis, and active control of vibration.

Ari Haavisto was born in Huittinen, Finland, in 1968. He received the B.Sc. degree in electrical engineering from Satakunta University of Applied Sciences, Pori, Finland, in 1994, and the M.Sc. degree in technology from Helsinki University of Technology, Espoo, Finland, in 2006.

He is Operations Engineer with the Department of Electrical Engineering, Faculty of Electronics, Communications, and Automation, School of Science and Technology, Aalto University, Espoo. His current research interests include thermal modeling of electric machines.

Antero Arkkio was born in Vehkalahti, Finland, in 1955. He received the M.Sc. degree in technology and the D.Sc. degree in technology from Helsinki University of Technology, Espoo, Finland, in 1980 and 1988, respectively.

He has been working with various research projects dealing with modeling, design, and measurement of all manner of electric machines. He served first as Senior Research Scientist, then as Laboratory Manager, and eventually Professor of electrical engineering at Helsinki University of Technology, Espoo. He is Professor of electrical engineering with the School of Science and Technology, Aalto University, Espoo.